Ceramics International xxx (xxxx) xxx

Contents lists available at ScienceDirect

Ceramics International

journal homepage: www.elsevier.com/locate/ceramint

A sol-gel templating route for the synthesis of hierarchical porous calcium phosphate glasses containing zinc

Farzad Foroutan [a], Isaac Abrahams [b], Glen J. Smales [c,d], Nasima Kanwal [b], Roberto di Pasquale [a], Jonathan C. Knowles [e,f,g], Andrew J. Smith [h], Daniela Carta [a,*]

[a] School of Chemistry and Chemical Engineering, University of Surrey, Guildford, UK
[b] Department of Chemistry, Queen Mary University of London, Mile End Road, London, E1 4NS, UK
[c] Bundesanstalt für Materialforschung und –prüfung (BAM), Berlin, Germany
[d] Graz University of Technology, Institute for Inorganic Chemistry, Stremayrstraße 9/IV, 8010, Graz, Austria
[e] Division of Biomaterials and Tissue Engineering, University College London, London, UK
[f] Department of Nanobiomedical Science & BK21 PLUS NBM Global Research Center for Regenerative Medicine, Dankook University, Cheonan, Republic of Korea
[g] UCL Eastman-Korea Dental Medicine Innovation Centre, Dankook University, Cheonan, Republic of Korea
[h] Diamond Light Source Ltd, Diamond House, Harwell Science and Innovation Campus, Didcot, Oxfordshire, OX11 0DE, UK

ARTICLE INFO

Handling Editor: Dr P. Vincenzini

Keywords:
Sol-gel
Phosphate-based glasses
Mesoporous materials
Hierarchical porosity

ABSTRACT

Hierarchical porous phosphate-based glasses (PPG) have great potential in biomedicine. Micropores (pore size <2 nm) increase the surface area, mesopores (pore size 2–50 nm) facilitate the absorption and diffusion of therapeutic ions and molecules making them ideal controlled delivery systems, while macropores (pore size >50 nm) facilitate the movement and diffusion of cells and fluids. In addition, the bioresorbability of PPG allows for their complete solubility in body fluid, alongside simultaneous formation of new tissue. Making PPG via the traditional melt-quenching (MQ) synthesis method used for phosphate-based glasses (PG), is not straightforward. Hence, we present here a route for preparing such glasses using a combination of sol-gel (SG) and templating methods. Hierarchical PPG in the P_2O_5–CaO–Na_2O system with the addition of 1, 3 and 5 mol % of Zn^{2+} were prepared with pore dimensions ranging from the micro-to the macro scales using Pluronic 123 (P123) as a surfactant. The presence of micropores (0.30–0.46 nm), mesopores (1.75–9.35nm) and macropores (163–207 nm) was assessed via synchrotron-based Small-Angle X-ray Scattering (SAXS), with the presence of the latter two confirmed by Scanning Electron Microscopy (SEM). Structural characterisation performed using ^{31}P solid state magic angle spinning nuclear magnetic resonance (MAS NMR) and Fourier Transform Infrared (FTIR) spectroscopies shows the presence of Q^2, Q^1 and Q^0 phosphate species with a predominance of Q^1 species in all compositions. Dissolution studies in deionised (DI) water confirm that controlled release of phosphates, Ca^{2+}, Na^+ and Zn^{2+} is achieved over a period of 7 days. In particular, the release of Zn^{2+} is proportional to its loading, making its delivery particularly easy to control.

1. Introduction

Phosphate-based glasses (PG) are very promising materials for medical applications as they are bioresorbable, meaning they dissolve in physiological environments without releasing any toxic species, and are eventually totally replaced by new-grown tissue [1–3]. Being bioresorbable, PG are ideal materials for the controlled local delivery of therapeutic ions/molecules. In particular, antimicrobial agents can be incorporated into PG and slowly released as the glass degrades preventing biomaterial-related infections [3]. PG are traditionally prepared using the melt-quenching (MQ) technique, which consists of melting oxide powders at high temperatures, followed by rapid cooling to avoid crystallisation. PG prepared via MQ have been widely studied [4–6]. In particular, PG systems based on the ternary P_2O_5–CaO–Na_2O system, prepared via MQ, have been investigated for their bioactive properties [7,8]. The MQ process is not ideal due to the high temperatures required and the difficulty of introducing porosity into the glasses. To the knowledge of the authors, only one example of PPG microspheres has been reported, where spheroidisation was utilised on PG powders previously prepared via MQ by using an oxy/acetylene flame spray gun [9].

* Corresponding author.
E-mail address: d.carta@surrey.ac.uk (D. Carta).

https://doi.org/10.1016/j.ceramint.2024.07.180
Received 10 May 2024; Received in revised form 3 July 2024; Accepted 13 July 2024
Available online 14 July 2024

In this work, we have used an in-solution sol gel (SG) process to synthesise porous phosphate glasses (PPG) with hierarchical porosity. Such porous structures are considered advantageous in materials for medical applications [10]. The SG method is a much more versatile technique than MQ, allowing for the extension of the compositional range over which glasses can be prepared [11,12]. The SG process is a wet chemical bottom-up technique based on the hydrolysis and polycondensation of precursors in solution [13,14]. Gels can be shaped into many forms (monoliths, porous foams, fibres, spheres and thin films) which can be desirable for specific applications, for instance coatings on metal implants (*e.g.* titanium hip joints) [15]. In contrast to the MQ technique, the SG process offers homogeneous mixing of the reactants due to the use of precursors in solution leading to high purity, high surface area glasses. Most importantly, the SG method allows for the formation of porous glasses [16].

Among the porous glasses important in biomedical applications, those containing pores in the range 2–50 nm (mesopores) are of particular interest. In particular, mesoporous silicate glasses (MSG) (*e.g.* MCM-4, SBA-15 type) prepared via the SG method have been extensively studied for their peculiar properties, such as high surface area, quick bioactive response and biocompatibility [17,18]. The simultaneous presence of micro-, meso- and macropores (hierarchical porosity) has also been presented as an important property that extends the glass functionalities [19]. Micropores increase surface area, mesopores improve uptake and local release of ions and drugs and bioactivity, while macropores improve cell movement and vascularisation, essential properties in tissue engineering applications [10]. Hierarchical porosity allows multifunctionality and enhancement of specific therapeutic properties such as osteogenesis and angiogenesis [10].

The SG method is ideal for manufacturing porous glasses via templating (supramolecular) chemistry using non-ionic block copolymers as surfactants [17]. At the critical micellar concentration, block copolymers spontaneously organize (self-assemble) into specific-shaped micelles, with the shape and size being dependent upon the specific block copolymer used. Simultaneously, the phosphate oxide precursor, dissolved in an appropriate solvent (*e.g.* ethanol), undergoes a series of hydrolysis and condensation reactions forming amorphous nanoparticles dispersed in the liquid (sol). As a result of solvent evaporation, these nanoparticles progressively deposit on the surface of the micelles, grow and agglomerate forming a hybrid phase consisting of an inorganic oxide network and organic supramolecular building blocks (gel). The much higher porosity and surface area enhance the bioactivity of the mesoporous glasses; in particular, it has been found that mesoporous bioactive glasses accelerate the rate of hydroxyapatite (HA) formation providing an ideal support for cell growth and supply of nutrients [20]. This is particular important for bone regeneration applications. A mesoporous structure allows easy accessibility and diffusion of molecules in all directions and facilitates the absorption and controlled release of therapeutic metallic ions (TMI) or molecules. In addition, from a biocompatibility perspective, SG glasses show a higher bone bonding rate than MQ due to their peculiar texture and surface properties [21].

PG have the potential to be better systems to be used for controlled delivery than those based on silicates, due to their higher solubility. In contrast to the extensive work carried out on MSG, very little has been done on PPG. Very recently, porous ternary system P_2O_5–CaO–Na_2O and porous quaternary systems with the addition of copper oxide and strontium oxide have been presented by Foroutan *et al.* [22–24] The porous ternary system has been shown to have enhanced properties compared to the non-porous analogous system, in particular, in terms of kinetics of hydroxycarbonate apatite formation and Saos-2 osteosarcoma cell attachment and proliferation on the surface of PPG.

PPG in the quaternary system P_2O_5–CaO–Na_2O–CuO (1, 3 and 5 mol % of Cu ions) have been shown to have extended porosity (micro, meso and macro) with a surface area decreasing from 87 to 67 $m^2\ g^{-1}$ with increasing Cu ion content from 1 to 5 mol %. Solid state magic angle spinning nuclear magnetic resonance (MAS NMR) showed that PPG contain Q^1 and Q^2 groups with a % of Q^2 decreasing with increasing Cu ion content (% of Q^2 43.5, 23.9 and 32.3 for 1, 3 and 5 mol copper ions %, respectively). Copper release in DI water was shown to be dependent on copper loading, with a release of ~ 33, 20 and 8 ppm of Cu ions from PPG containing 1, 3 and 5 mol % of Cu ions content % after 7 days [23].

PPG in the quaternary system P_2O_5–CaO–Na_2O–SrO (1, 3 and 5 mol % of Sr ions) showed similar results to the P_2O_5–CaO–Na_2O–CuO in terms of the surface area decreasing from 112 to 73 $m^2\ g^{-1}$ with increasing Sr ion content from 1 to 5 mol % and dissolution in DI water (about 23, 15 and 7 ppm of Sr ions from PPG containing 1, 3 and 5 mol % of Sr ions, after 7 days). Solid state MAS NMR showed that PPG contain mainly Q^1 and Q^2 groups, about 60 to 40 %, respectively which do not change much with Sr^{2+} content [24]. Apart from this pioneering work, very little has been reported on the synthesis of PPG.

Here, the SG method combined with supramolecular templating has been used for the production of PPG with the addition of Zn^{2+}. The addition of Zn^{2+} to PG prepared via MQ has been shown to bestow the glasses with antibacterial potential as well as osteoconductive properties [25,26]. In this work, we demonstrate the feasibility of the SG-templating route for the synthesis of Zn-containing PPG with extended porosity using the surfactant P123. A detailed analysis of the porous structure was performed via synchrotron-based small angle X-ray scattering (SAXS), Scanning Electron Microscopy (SEM) and adsorption-desorption analysis of N_2 at 77 K. An atomic scale structural analysis was performed via investigation of the phosphorus environment via ^{31}P MAS-NMR and Fourier Transform Infrared spectroscopy (FTIR). Finally, the controlled release of phosphates, Ca^{2+}, Na^+ and Zn^{2+} in DI water was investigated.

2. Experimental

2.1. Synthesis

The following chemical precursors were used without further purification: n-butyl phosphate (1:1 molar ratio of mono $OP(OH)_2(OBu^n)$ and di-butyl phosphate $OP(OH)(OBu^n)_2$, Alfa Aesar, 98 %), calcium methoxyethoxide (CaMeOEt, ABCR, 20 % in methoxyethanol), sodium methoxide (NaOMe, Aldrich, 30 wt% in methanol), zinc acetate (Zn-acetate, Aldrich, 98 %), ethanol (EtOH, Fisher, 99 %), and Pluronic 123 (P123 – M_n = 5800 g mol^{-1}, Aldrich).

The reason why a 1:1 molar ratio of mono and di-butyl phosphate is used is because it has been found to be an ideal precursor for gel formation. It has been show that the hydrolysis of phosphate esters, $PO(OR)_3$ is too slow and that of phosphoric acid is too high usually leading

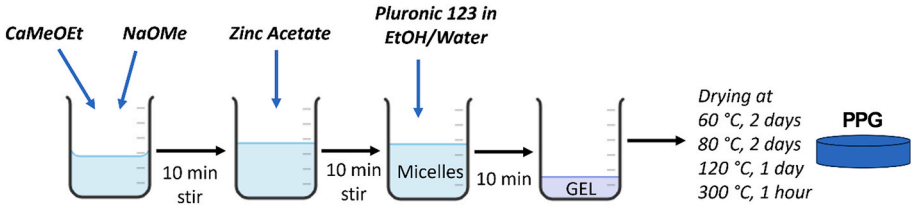

Fig. 1. Schematic of the sol-gel method used for the synthesis of PPG containing Zn.

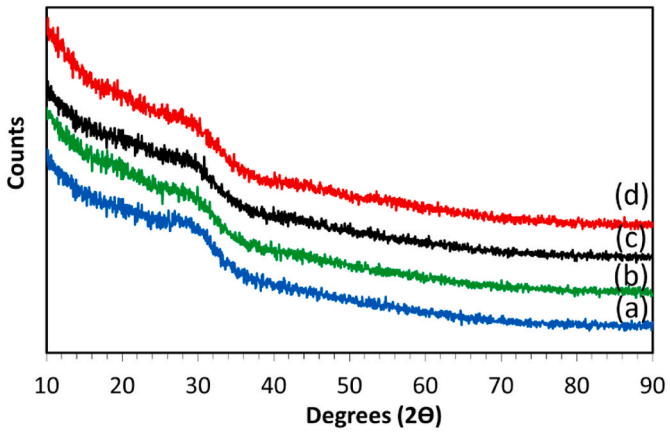

Fig. 2. XRD patterns of (a) PPG-und, (b) PPG-Zn1, (c) PPG-Zn3, (d) PPG-Zn5.

to precipitation instead of gelation [10,12].

The ternary PPG in the system P_2O_5–CaO–Na_2O was prepared by adding 1.7 g of n-butyl phosphate to 5 mL of EtOH in a dry beaker under stirring for 10 min. 3.5 g of CaMeOEt and 0.5 g of NaOMe were then added dropwise into the mixture while stirring; the solution was kept stirring for about 1 h. The quaternary PPG in the system P_2O_5–CaO–Na_2O–ZnO containing 1, 3, or 5 mol % of Zn^{2+} were prepared by adding 0.03, 0.10, and 0.16 g of Zn-acetate and 0.49, 0.47 and 0,44 g of NaOMe into the mixture, respectively. In each case, the mixture was left stirring for further 10 min. Finally, a solution consisting of 3.0 g of P123, 5 mL of EtOH and 2.5 mL of DI water was added to the mixture and allowed to react for further 10 min. The mixtures were poured into suitable PTFE containers and gelation occurred after about 5 min. Gels were then left to stand in the same container at room temperature for 24 h. Gels were then progressively dried by heating them at 60 °C for 2 days, at 80 °C for 2 days, and finally at 120 °C for 1 day. The dried powders were then heated to 300 °C at a rate of 1 °C · min^{-1} and calcined at this temperature for 1 h. The powders were then ground using a MM301 mill at 10 Hz (Retsch GmbH, Hope, UK) and sieved in the size range of 106–200 μm (Endecotts Ltd, London, UK). A schematic of the SG preparation of Zn-containing PPG is presented in Fig. 1. Glasses will be hereafter indicated as PPG-und (ternary system Zn-free) and PPG-ZnX (quaternary systems with added Zn) where X = mol % Zn.

2.2. Structural characterization

X-ray powder diffraction (XRD, PANalytical X'Pert, Royston, UK) was performed on powdered samples in flat plate θ/θ geometry using Ni filtered Cu Kα radiation. Data were collected using a PIXcel^{1D} detector over a 2θ range of 10–90° with a step size of 0.05° and a time per step of 12 s.

SAXS measurements were conducted using the MOUSE instrument (Bundesanstalt für Materialforschung und –prüfung (BAM), Berlin, Germany) [27]. X-rays were generated from a microfocus X-ray tube, followed by multilayer optics to parallelize and monochromatize the X-ray beam to the Cu Kα wavelength (λ = 0.154 nm). Scattered radiation was detected on an in-vacuum Eiger 1 M detector (Dectris, Switzerland), which was placed at multiple distances between 138 and 2507 mm from the sample. The resulting data were processed and scaled using the DAWN software package in a standardized, complete 2D correction pipeline with uncertainty propagation [28,29]. The data were subsequently fitted and analysed using McSAS, a Monte Carlo method to extract form-free size distributions [30]. McSAS uses a Monte Carlo approach to generate particle size distributions, where for each distribution, a scattering pattern is simulated and compared to the experimental data. The distributions are then iteratively refined to achieve good agreement between the simulated and experimental data. This process is then repeated multiple times to provide form-free size distributions with error estimations.

SEM images were acquired with a JSM-7100F instrument (Jeol, Welwyn, UK) with an accelerating voltage of 10.0 kV. The samples were mounted onto aluminium stubs using carbon conductive tape. Carbon coating was used to reduce sample charging. Pore sizes were measured using the Image-pro plus software (Media Cybernetics, USA). The exact composition of the glasses was evaluated using Energy Dispersive X-ray Spectroscopy (EDX, MagnaRay, ThermoFisher, Hemel Hempstead, UK) performed using SEM operating at 20.0 kV.

N_2 adsorption-desorption analysis at 77 K was performed on a Gemini V instrument (Micromeritics, Hertfordshire, UK). The specific surface area was assessed using the Brunauer-Emmet-Teller (BET) method.

Solid-state ^{31}P MAS-NMR spectra (AVANCE III 600, Bruker, Coventry, UK) were recorded at 242.938 MHz using direct excitation with a 90° pulse and 60 s recycle delay at ambient probe temperature (~25 °C). Powdered samples were loaded into 4.0 mm outer diameter zirconia rotors, spun at 12 kHz, and for each sample 16 scans were acquired. Spectra were referenced to 85 % H_3PO_4 solution at 0 ppm. The centre band resonances were fitted using the Dmfit software package [31].

FTIR spectra were acquired using an FTIR-2000 instrument (PerkinElmer, Seer Green, UK) equipped with Timebase software and an attenuated total reflectance accessory (Golden Gate, Specac, Orpington, UK) in the range of 4000–600 cm^{-1}.

2.3. Dissolution study

Dissolution products were obtained by immersing 10 mg of each sieved PPG powder in 10 mL of DI water for 1, 3, 5, and 7 days. The experiments were carried out in triplicate (n = 3). The resulting suspensions for each time point were then centrifuged at 4800 rpm for 10 min to separate the PPG powders from the solution. The released phosphates, Ca^{2+}, Na^+ and Zn^{2+} in solution were then measured via ICP-OES (720 ES-Varian, Crawley, UK). Calibration across the expected concentration range was performed using standard solutions (ICP multi-element standard solution, VWR). All samples and standards were diluted in a 1:1 ratio with 4 % HNO_3 (Honeywell, Fluka™) and a blank solution (2 % HNO_3) was used as a reference under standard operating conditions.

Table 1
Compositions of the PPG measured by EDX expressed in terms of atomic %, with expected values based on starting composition given in parentheses.

Glass Code	Elements (atomic %)				
	O	P	Ca	Na	Zn
PPG-und	69.8 ± 0.4 (63.1)	15.0 ± 0.1 (20.3)	7.1 ± 0.1 (8.1)	8.1 ± 0.1 (8.6)	–
PPG-Zn1	67.4 ± 0.4 (63.1)	16.2 ± 0.1 (20.1)	11.6 ± 0.1 (8.7)	5.27 ± 0.1 (7.8)	0.47 ± 0.1 (0.3)
PPG-Zn3	68.6 ± 0.4 (63.6)	16.1 ± 0.1 (20.5)	8.2 ± 0.1 (8.2)	6.30 ± 0.3 (7.2)	0.77 ± 0.1 (0.5)
PPG-Zn5	60.9 ± 0.4 (63.9)	19.7 ± 0.1 (20.5)	11.9 ± 0.1 (8.8)	5.25 ± 0.4 (5.8)	2.30 ± 0.2 (1.0)

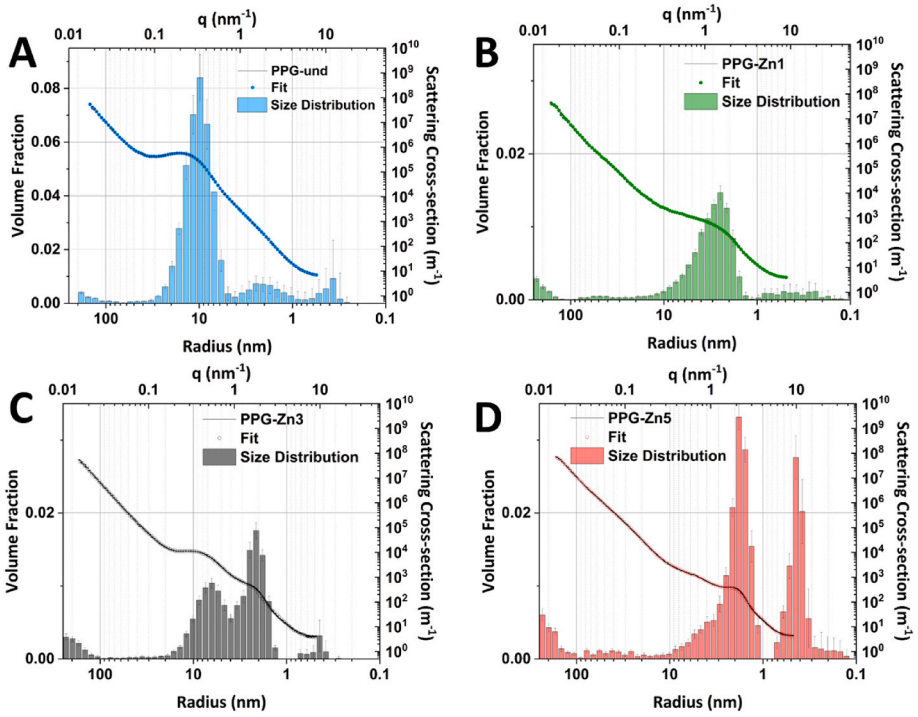

Fig. 3. Fitted SAXS data for: (A) PPG-und, (B) PPG-Zn1, (C) PPG-Zn3, (D) PPG-Zn5.

3. Results and discussion

3.1. X-ray diffraction

The XRD patterns, reported in Fig. 2, indicate that all samples are fully amorphous with no Bragg peaks evident and only a broad halo centered at around 2θ ~27°, characteristic of the amorphous phosphate network. The results confirm that the calcination at 300 °C and the addition of up to 5 mol % of Zn^{2+} do not induce crystallisation.

3.2. Chemical analysis

SEM imaging combined with EDX analysis was used to identify the chemical composition of PPG after calcination at 300 °C. The reason why calcination was performed at 300 °C is that higher temperatures might have caused crystallisation or collapse of the porous structure. PG have a very small processing window between the loss of organics from the structure and the softening temperature at which the glass collapses [31].

Elemental compositions expressed in terms of atomic % and oxide mol % are reported in Table 1 and Table SI-1, respectively. Targeted compositions were selected on the basis of previous studies on undoped MQ and SG prepared PG; glasses with P_2O_5 and CaO contents in the range of 40–55 mol % and 30–40 mol %, respectively, have shown good bioactivity and biocompatibility. As shown in Table 1, the observed values differ significantly from those expected from the starting compositions. Such deviation away from the starting composition is similar to that seen in Sr and Cu loaded PPG prepared via SG [23,24]. This can be explained considering the role of the surfactant P123, used as templating agent in the preparation of the PPG systems. The presence of residual carbon leads to formation of P–O–C linkages causing the O:P ratio to be higher than that expected from the starting composition (apart from the PPG-Zn5 composition where the O:P ratio of 3.1 is close to that expected). The phosphate network is broken up by the formation of P–O–C linkages with the P123 chain. This leads to a decrease in condensation of the phosphate network with a consequent increase in the O:P ratio. The observed Na:Zn ratios are all higher than those expected, while the Ca:Zn ratios are all lower than expected. Nevertheless, the glasses show increasing Zn incorporation with increasing Zn loading in the starting compositions.

Table 2
Mean radii of pore populations in nm from PPG derived from fits of SAXS data using Monte Carlo methods.

Population	Size distribution range (nm)			
	PPG-und	PPG-Zn1	PPG-Zn3	PPG-Zn5
1	0.46 ± 0.07	0.30 ± 0.01	0.43 ± 0.02	0.46 ± 0.03
2	2.00 ± 0.03	2.44 ± 0.01	2.01 ± 0.05	1.75 ± 0.02
3	9.35 ± 0.47	–	7.88 ± 0.12	–
4	163.36 ± 4.61	186.35 ± 1.11	206.93 ± 1.5	202.29 ± 2.48

3.3. Small-Angle X-ray scattering

SAXS is one of the few techniques suitable for studying the structure of porous materials in the range from 1 to around 400 nm, which makes it an ideal technique for the investigation of hierarchical porous materials [32]. One advantage of SAXS is that it is also possible to obtain information on pore systems that may not be accessible via sorption measurements, as the method probes the electron density contrast within a material, rather than relying upon permeable access to the pore systems [33]. All SAXS data were collected and subsequently analysed, using Monte Carlo methods, for each PPG and are presented in Fig. 3. Each PPG shows the presence of hierarchical structures, with the simultaneous presence of micro-, meso- and macropores to some degree (Table 2). The graphs show the SAXS data and fits on top of the resultant histograms of the fits, displaying the obtained structural size distributions.

For each PPG, the SAXS data show an upturn in the scattering signal towards low-q, which indicates the presence of larger structures (*e.g.* larger pores or grain boundaries). This is represented in the McSAS fit results by population 4 in Table 2, the values of which should only be considered as rough estimates of the size of these structures as they are too large to be observed clearly using conventional SAXS methods.

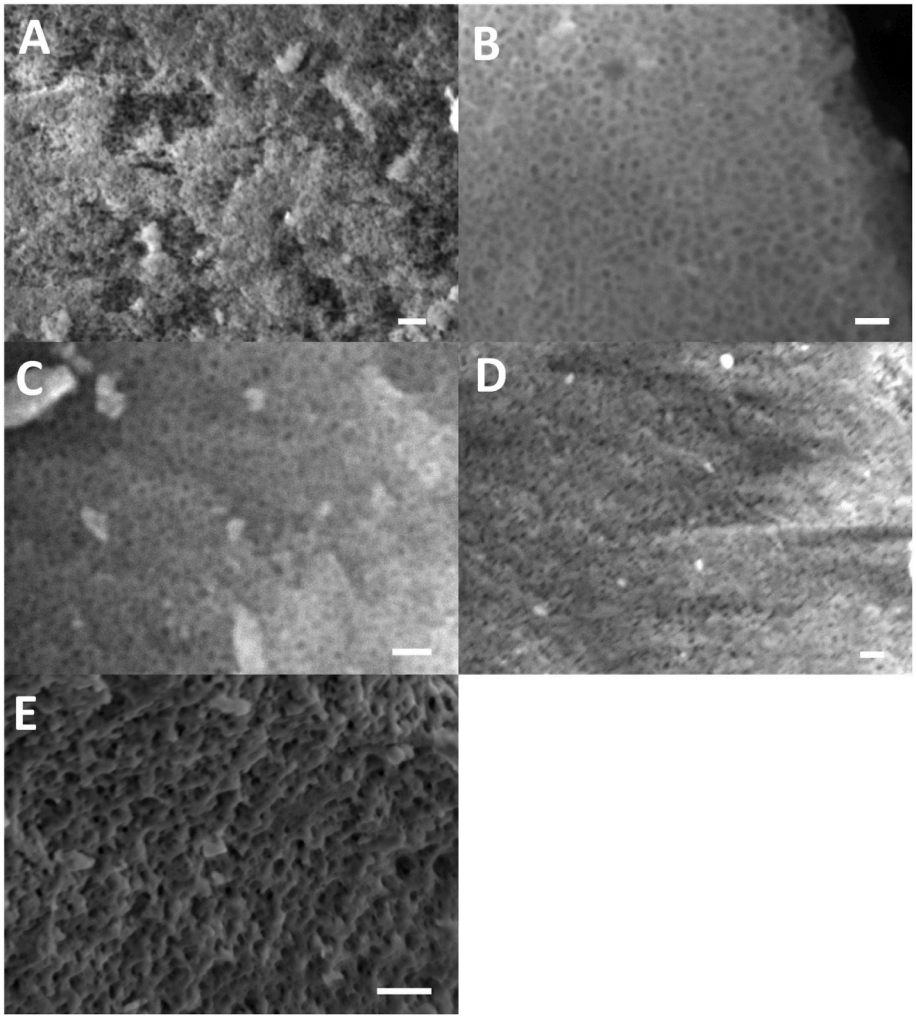

Fig. 4. SEM images of (A) PPG-und, (B) PPG-Zn1, (C) PPG-Zn3, (D and E) PPG-Zn5. Scale bar A–D: 200 nm; E 1 μm.

Monte Carlo fits of the SAXS data for PPG-und show a primary population of pores with an average radius of 9.35 nm (Table 2, population 3). Alongside this primary population, are two smaller populations (in terms of, both, volume fraction and size) with average radii of 2.00 and 0.46 nm (population 2 and 1 in Table 2, respectively). With the addition of 1 mol % Zn (PPG-Zn1) the resulting primary population is decreased in average radius to ~ 2.44 nm and occupies a decreased overall volume fraction. With increasing Zn content, the primary population appears to become bimodal, with average radii of 2.01 and 7.88 nm for PPG-Zn3, which then become monomodal again with an average pore radius of 1.75 nm for PPG-Zn5. This change for PPG-Zn5 also comes with a drastic increase in microporosity with an average pore radius of 0.46 nm. It is important to note that for all PPGs, <1 nm micropores are observed, which is a common observation in ordered materials templated with P123 (*e.g.* SBA-15 and COK-12) and are thought to indicate inter-channel porosity [34–36].

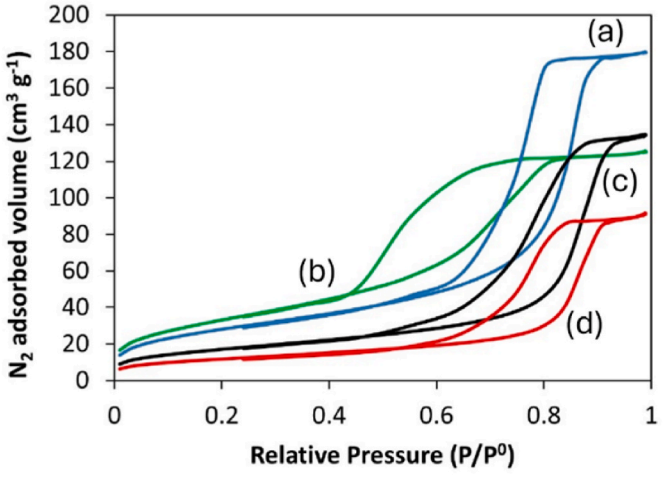

Fig. 5. N_2 adsorption-desorption isotherms at 77 K of (a) PPG-und, (b) PPG-Zn1, (c) PPG-Zn3, (d) PPG-Zn5.

When comparing the Zn containing samples, the abundance, and narrowness of the size distribution, dramatically increases from PPG-Zn1 and PPG-Zn3 to PPG-Zn5. This observed increase in the volume fraction could indicate the presence of some hexagonal order within the system. If the bump around ~ $q = 2\ nm^{-1}$, is considered to be from a hexagonal lattice, this would give a pore-to-pore half distance of ~ $a =$ 1.8 nm which lines up well with the equivalent radial value observed from the McSAS analysis of 1.75 nm in PPG-Zn5 (population 2, Table 2). The presence of some hexagonal domains is also supported by the increased microporosity observed in the SAXS data.

Simulations of SAXS curves from 3D models of hexagonal lattices have previously been utilised to understand the relationship between individual parameters describing a hexagonal lattice and the resultant scattering, and how such curves change when transitioning from an ordered hexagonal lattice to a more disordered material [35,37]. Such

Table 3
Textural properties of PPG derived from N_2 adsorption/desorption isotherms.

Sample code	Surface area ($m^2.g^{-1}$)	Pore size (nm)
PPG-und	123 ± 6	11.8 ± 0.6
PPG-Zn1	92 ± 5	11.3 ± 0.6
PPG-Zn3	82 ± 4	12.1 ± 0.6
PPG-Zn5	76 ± 4	11.7 ± 0.6

reported simulations, provide some insight into how some domains of more-ordered material may be present for the materials reported here, especially when considering that it is expected for the P123 template to arrange hexagonally. Such domains with some longer-range order may also not be accessible to sorption methods, hence the relatively low surface area reported below.

3.4. Scanning Electron Microscopy

Using the surfactant templating technique, the removal of the organic micelles of surfactant P123 by calcination results in a highly porous structure. This is confirmed by the SEM images presented in Fig. 4A–D and Figs. SI–1, which show extended mesoporosity in all PPG, comparable with MSG systems prepared using P123 as a surfactant [38]. It has to be noted that mesopore structure would be better visualised using the higher resolution transmission electron microscopy (TEM) technique instead of SEM. However, beam damage occurs on PPG while imaging using TEM with collapse of the porous structure. Mesopore sizes estimated using SEM images have average dimensions of 10–30 nm. These results confirm that PPG can be obtained similarly to MSG using P123. However, macroporosity can also be observed with pore sizes in the range 200–450 nm (Fig. 4E), in agreement with SAXS data.

3.5. Adsorption-desorption of N_2 at 77 K

The surface area of all PPG was measured using adsorption-desorption of N_2 at 77 K. The N_2 adsorption-desorption isotherms of all PPG are shown in Fig. 5. All glasses show isotherms with a hysteresis loop starting at $P/P_0 \sim 0.45$ which confirms the presence of mesopores. The isotherms are classified as type IV and arise from capillary condensation and evaporation in mesoporous materials. This process give rise to hysteresis loops the shapes of which indicate a particular geometry of mesopores. PPG-und clearly shows a type H1 loop which is indicative of a cylindrical mesopores with a narrow size distribution [37]. This was expected as the block copolymer surfactant used (P123) is known to form cylindrical micelles, which aggregate forming two dimensional hexagonal arrangements. Zn-containing PPG show distorted hysteresis loops, nevertheless compatible with the presence of mesopores.

Surface areas calculated using the BET model are reported in Table 3, along with the pore sizes. The highest surface area (123 $m^2\ g^{-1}$) was observed for the PPG-und sample with an average pore size ~ 12 nm. The surface area decreases, as the Zn^{2+} loading increases, reaching the lowest value of 76 $m^2\ g^{-1}$ for the PPG-Zn5 sample. No significant changes were observed in pore sizes on increasing the Zn^{2+} content, in agreement with the previously investigated Sr^{2+} containing PPG [24].

3.6. ^{31}P MAS NMR

The structure of the phosphate network of all PPG was studied using solid state ^{31}P MAS NMR. Resonances were assigned using the Q^n notation, where n represents the number of bridging oxygens between phosphates units. Spectra are presented in Fig. 6A, compositional variation of isotropic chemical shifts are reported in Fig. 6B and the spectral

Table 4
^{31}P MAS-NMR spectral parameters (chemical shift, δ_{iso}) and relative intensity (I %) obtained by signal deconvolution (estimated error = ±5 %).

	Q^0		Q^1		Q^2	
	δ_{iso} (ppm)	**I (%)**	**δ_{iso} (ppm)**	**I (%)**	**δ_{iso} (ppm)**	**I (%)**
PPG-und	1.33	5.50	−7.44	70.00	−21.09	24.50
PPG-Zn1	0.61	10.12	−7.69	75.83	−20.28	14.05
PPG-Zn3	0.68	7.12	−7.73	71.17	−20.61	21.72
PPG-Zn5	0.66	7.55	−7.73	69.25	−20.39	23.20

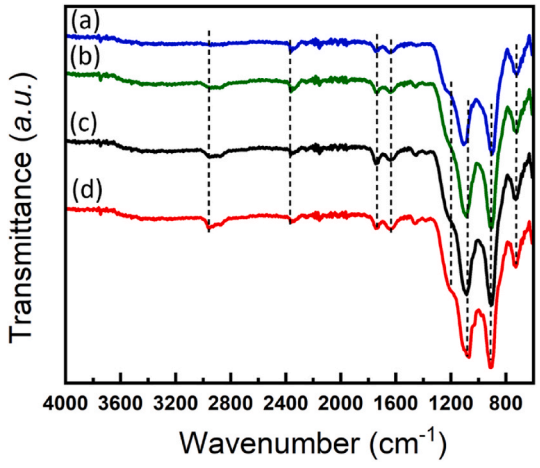

Fig. 7. FTIR spectra of (a) PPG-und, (b) PPG-Zn1, (c) PPG-Zn3 and (d) PPG-Zn5.

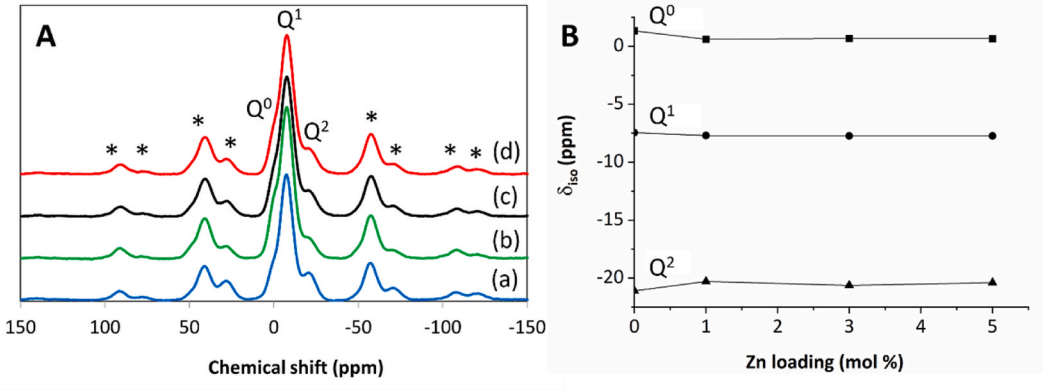

Fig. 6. A) ^{31}P MAS NMR spectra of (a) PPG-und, (b) PPG-Zn1, (c) PPG-Zn3 and (d) PPG-Zn5, with spinning side bands denoted by asterisks; B) compositional variation of isotropic chemical shift.

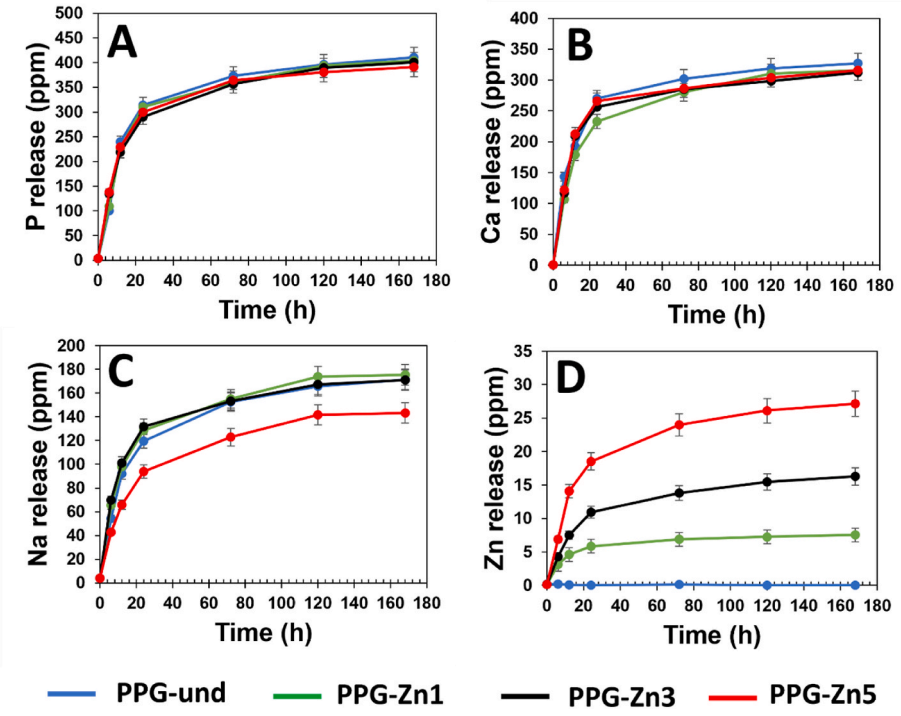

Fig. 8. Release of **(A)** phosphorus, **(B)** calcium, **(C)** sodium and **(D)** zinc species in DI water up to 7 days by ICP-OES. Error bars are standard deviations (n = 3).

parameters are reported in Table 4.

The main resonances observed correspond to Q^1 groups in the range from −7.44 to −7.73 ppm, Q^2 groups in the range from −20.28 to −21.09 ppm and Q^0 groups in the range from 0.66 to 1.33 ppm.

The ^{31}P MAS NMR spectra show that Q^1 is the dominant species in all PPG compositions. This result is consistent with other PPG systems prepared via SG containing strontium [24] and copper ions [23] and PG containing Cu ions prepared using an in solution-single step technique [39]. As discussed above, the lower degree of network condensation (*i.e.* higher O:P ratio) than would be expected from the starting composition can be explained considering that the surfactant P123 has been used as templating agent in the preparation of the PPG systems. This leads to a breaking of P–O–P linkages and the formation of P–O–C linkages between the phosphate network and the P123 chains. The consequence of this is a decrease in condensation of the phosphate network with an increase in the O:P ratio.

3.7. Fourier Transform Infrared spectroscopy (FTIR)

The FTIR spectra of all PPG are reported in Fig. 7. The bands arising from the vibrations of the phosphate network appear in the range 1400–600 cm^{-1}. Bands due to the vibrations of Q^2 (P–O–P) groups were observed at ~720 cm^{-1} symmetrical stretching mode υ_s(P–O–P) and at ~ 900 cm^{-1} asymmetrical stretching mode υ_{as}(P–O–P). Vibrations due to Q^1 units assigned to asymmetrical $\upsilon_{as}(PO_3)^{2-}$ modes are also observed at ~1104 cm^{-1} for PPG-und and shift up to ~1072 cm^{-1} for PPG-Zn5. It should be noted that the stretching wavenumbers (and therefore the stretching frequencies) of non-bridging P–O_T groups are higher than the ones for bridging P–O_B, indicating that the P–O_T bond is shorter than P–O_B, as proved by neutron diffraction experiments [25]. The shoulder at 1244 cm^{-1} for PPG-und is assigned to the $\upsilon_{as}(PO_2)$ mode and also shifts up to 1200 cm^{-1} on varying the composition up to PPG-Zn5. The peak at 1460 cm^{-1} can be assigned to P–O double bond symmetric stretching. The band at ~2340 cm^{-1} is due to adsorbed CO_2. A very wide, low intensity band is observed in the range 3200–3400 cm^{-1} (symmetric stretching) and around 1640 cm^{-1} (bending) due to O–H groups of water molecules, δ(H–O–H) [23]. Weak signals due to the stretching of the C–H groups of residual organics υ(C–H), are visible at around 2900 cm^{-1}. The presence of residual carbon is very common in manufacturing glasses using the sol-gel process. However, C does not negatively affect the bioactive properties. It has been reported that calcium phosphate scaffolds for bone regeneration containing residual carbon exhibited improved reactivity in simulated body fluid. However, the presence of C resulted in a lower densification of the scaffolds and, subsequently, poorer mechanical performance under compressive stresses [40].

3.8. Dissolution study

The degradation of all PPG in DI water was studied over a period of 7 days. The concentrations of all ionic species released were analysed and quantified. The release profiles of phosphates, Ca^{2+}, Na^+, and Zn^{2+}, identified via ICP-OES, are reported in Fig. 8.

The release profiles of Ca^{2+} do not change significantly with zinc loading over the entire period of 7 days. This is consistent with what has been recently observed in PPG-Cu and PPG-Sr containing systems prepared via SG. Values start from ~ 120 ppm (6h), 200 ppm (12 h), 250 ppm (24 h), 280 (72 h) and 300 ppm (120 h) up to 330 ppm at 168 h. The overall amount of Ca^{2+} released after 7 days is also consistent with that seen in Cu/Sr doped systems [23,24].

The release profiles of Na^+ are similar for PPG-und, PPG-Zn1 and PPG-Zn3 glasses but that for PPG-Zn5 shows lower overall release. After 7 days, the maximum Na^+ released is around 170 ppm by PPG-und, PPG-Zn1 and PPG-Zn3 glasses whereas that for the PPG-Zn5 glass is 143 ppm. This is also in agreement with PPG-Cu and PPG-Sr systems previously presented, for which the lowest Na^+ release was observed for glasses containing 5 mol % of Cu/Sr. However, a more consistent decrease in solubility with TMI content was observed for the Cu/Sr containing PPG [23,24].

The release of phosphates also does not change significantly with increasing Zn loading, whereas in the PPG containing Cu and Sr a higher TMI content corresponded to a lower phosphates release. These results seem to indicate that the phosphate chains in the glasses are not significantly affected by the addition of Zn^{2+}. The maximum release is

400 ppm after 7 days. As expected, the release of zinc is dependent on its content, clearly increasing with the zinc loading as observed for the Cu and Sr containing PPG. The dose dependent release of zinc is also seen in day one, in contrast to the release of all other ions. Zn release concentrations after 7 days are ~ 7, 16 and 27 ppm for PPG-Zn1, PPG-Zn3 and PPG-ZN5, respectively.

4. Conclusions

Hierarchical P_2O_5–CaO–Na_2O PPG with the addition of 1, 3 and 5 mol % of Zn^{2+} have been successfully synthesized using a combination of SG and templating methods using P123 as a surfactant. The presence of micropores, mesopores and macropores has been confirmed via SAXS analysis, while that of mesopores and macropores has been further confirmed via SEM imaging. N_2 adsorption-desorption analysis reveals mesopores with an average pore size of ~12 nm. Addition of Zn up to 5 mol % does not significantly affect the size of the mesopores; however, the surface area is affected, decreasing from 124 $m^2\ g^{-1}$ in the Zn free PPG to 76 $m^2\ g^{-1}$ in the PPG with the highest Zn loading. ^{31}P MAS NMR shows that PPG contain predominantly Q^1 phosphate species, well above that expected from the starting composition, but in line with other SG prepared PPG. The release of phosphates, Ca^{2+}, Na^+ and Zn^{2+} in DI water was studied via ICP-OES analysis over a period of 7 days. The release of Zn^{2+} increases proportionally to its loading, making the PPG particularly interesting as controlled delivery systems.

CRediT authorship contribution statement

Farzad Foroutan: Writing – original draft, Investigation, Formal analysis. **Isaac Abrahams:** Writing – review & editing, Validation. **Glen J. Smales:** Writing – review & editing, Visualization, Formal analysis, Data curation. **Nasima Kanwal:** Writing – review & editing, Validation. **Roberto di Pasquale:** Investigation. **Jonathan C. Knowles:** Writing – review & editing, Validation, Methodology. **Andrew J. Smith:** Investigation. **Daniela Carta:** Writing – review & editing, Writing – original draft, Validation, Supervision, Conceptualization.

Declaration of competing interest

The authors declare that they have no known competing financial interests or personal relationships that could have appeared to influence the work reported in this paper.

Acknowledgments

The authors would like to acknowledge EPSRC (EP/P033636/1, EP/T023740/1), the Royal Society of Chemistry (R21-7668912428) and the Royal Society (RSG\R1\180191) for providing the funding to conduct this study. The authors are also grateful to Dr David Jones (Microstructural Studies Unit, University of Surrey) for his help with the SEM/EDX, Dr Daniel Driscoll for his help with XRD and Dr Rachida Bouce-Soualhi for her assistance with FTIR (University of Surrey) and Dr Graham Palmer for his help with ICP-OES measurements (UCL). DC thanks the University of Surrey and ICase NPL for funding RDP's PhD studentship. We are grateful to Harold Toms at Queen Mary University of London for his help in NMR data collection. We gratefully acknowledge the Diamond Light Source for time on Beamline I22 under Proposals SM21476 and SM27911.

Appendix A. Supplementary data

Supplementary data to this article can be found online at https://doi.org/10.1016/j.ceramint.2024.07.180.

References

[1] E.A. Abou Neel, V. Salih, J.C. Knowles, Phosphate-based glasses, Compr. Biomater. 1 (2011) 285–297, https://doi.org/10.1016/B978-0-08-055294-1.00249-X.
[2] D. Carta, D.M. Pickup, F. Foroutan, Chapter 6: phosphate-based Glasses prepared via sol-gel and coacervation, in: Obata Akiko, S. Brauer Delia, Kasuga Toshihiro (Eds.), Phosphate and Borate Bioactive Glasses, 2022, pp. 78–113, https://doi.org/10.1039/9781839164750.
[3] N.J. Lakhkar, I.-H. Lee, H.-W. Kim, V. Salih, I.B. Wall, J.C. Knowles, Bone formation controlled by biologically relevant inorganic ions: role and controlled delivery from phosphate-based glasses, Adv. Drug Deliv. Rev. 65 (2013) 405–420, https://doi.org/10.1016/J.ADDR.2012.05.015.
[4] I. Ahmed, E.A. Abou Neel, S.P. Valappil, S.N. Nazhat, D.M. Pickup, D. Carta, D. L. Carroll, R.J. Newport, M.E. Smith, J.C. Knowles, The structure and properties of silver-doped phosphate-based glasses, J. Mater. Sci. 42 (2007) 9827–9835, https://doi.org/10.1007/s10853-007-2008-9.
[5] I. Ahmed, D. Ready, M. Wilson, J.C. Knowles, Antimicrobial effect of silver-doped phosphate-based glasses, J. Biomed. Mater. Res. 79 (2006) 618–626, https://doi.org/10.1002/jbm.a.30808.
[6] N.B. Hyunh, C.S.D. Palma, R. Rahikainen, A. Mishra, L. Azizi, E. Verne, S. Ferraris, V.P. Hytönen, A. Sanches Ribeiro, J. Massera, Surface modification of bioresorbable phosphate glasses for controlled protein adsorption, ACS Biomater. Sci. Eng. 7 (2021) 4483–4493, https://doi.org/10.1021/acsbiomaterials.1c00735.
[7] I. Ahmed, M. Lewis, I. Olsen, J.C. Knowles, Phosphate glasses for tissue engineering: part 1. Processing and characterisation of a ternary-based P_2O_5–CaO–Na_2O glass system, Biomaterials 25 (2004) 491–499, https://doi.org/10.1016/s0142-9612(03)00546-5.
[8] J.C. Knowles, Phosphate based glasses for biomedical applications, J. Mater. Chem. 13 (2003) 2395–2401, https://doi.org/10.1039/b307119g.
[9] K.M.Z. Hossain, U. Patel, A.R. Kennedy, L. Macri-Pellizzeri, V. Sottile, D.M. Grant, B.E. Scammell, I. Ahmed, Porous calcium phosphate glass microspheres for orthobiologic applications, Acta Biomater. 72 (2018) 396–406, https://doi.org/10.1016/j.actbio.2018.03.040.
[10] F. Baino, S. Fiorilli, C. Vitale-Brovarone, Bioactive glass-based materials with hierarchical porosity for medical applications: review of recent advances, Acta Biomater. 42 (2016) 18–32, https://doi.org/10.1016/j.actbio.2016.06.033.
[11] D. Carta, J.C. Knowles, M.E. Smith, R.J. Newport, Synthesis and structural characterization of P_2O_5–CaO–Na_2O sol-gel materials, J. Non-Cryst. Solids 353 (2007) 1141–1149, https://doi.org/10.1016/j.jnoncrysol.2006.12.093.
[12] J. Livage, P. Barboux, M.T. Vandenborre, C. Schmutz, F. Taulelle, Sol-gel synthesis of phosphates, J. Non-Cryst. Solids 148 (1992) 18–23, https://doi.org/10.1016/S0022-3093(05)80586-1.
[13] I.-H. Lee, F. Foroutan, N.L. Lakhkar, M.-S. Gong, J.C. Knowles, Sol-gel synthesis and structural characterization of P_2O_5–CaO–Na_2O glasses, Phys. Chem. Glasses: Eur. J. Glass Sci. Technol. B 54 (2013) 115–120.
[14] F. Foroutan, N.H. de Leeuw, R.A. Martin, G. Palmer, G.J. Owens, H.W. Kim, J. C. Knowles, Novel sol–gel preparation of $(P_2O_5)_{0.4}$–$(CaO)_{0.25}$–$(Na_2O)_X$–$(TiO_2)_{(0.35-X)}$ bioresorbable glasses (X = 0.05, 0.1, and 0.15), J. Sol. Gel Sci. Technol. 73 (2014) 434–442, https://doi.org/10.1007/s10971-014-3555-6.
[15] L.L. Hench, J.R. Jones, Bioactive glasses: frontiers and challenges, Front. Bioeng. Biotechnol. 3 (2015) 1–12, https://doi.org/10.3389/fbioe.2015.00194.
[16] M. Vallet-Regí, Ordered mesoporous materials in the context of drug delivery systems and bone tissue engineering, Chem. Eur J. 12 (2006) 5934–5943, https://doi.org/10.1002/chem.200600226.
[17] M. Vallet-regi, A.J. Salinas, Mesoporous bioactive glasses for regenerative medicine, Mater. Today Bio. 11 (2021) 100121, https://doi.org/10.1016/j.mtbio.2021.100121.
[18] M. Manzano, M. Vallet-Regí, New developments in ordered mesoporous materials for drug delivery, J. Mater. Chem. 20 (2010) 5593–5604, https://doi.org/10.1039/b922651f.
[19] C. Wu, W. Fan, Y. Zhu, M. Gelinsky, J. Chang, G. Cuniberti, V. Albrecht, T. Friis, Y. Xiao, Multifunctional magnetic mesoporous bioactive glass scaffolds with a hierarchical pore structure, Acta Biomater. 7 (2011) 3563–3572, https://doi.org/10.1016/J.ACTBIO.2011.06.028.
[20] A. López-Noriega, D. Arcos, I. Izquierdo-Barba, Y. Sakamoto, O. Terasaki, M. Vallet-Regí, Ordered mesoporous bioactive glasses for bone tissue regeneration, Chem. Mater. 18 (2006) 3137–3144, https://doi.org/10.1021/cm060488o.
[21] G.J. Owens, R.K. Singh, F. Foroutan, M. Alqaysi, C.M. Han, C. Mahapatra, H. W. Kim, J.C. Knowles, Sol-gel based materials for biomedical applications, Prog. Mater. Sci. 77 (2016) 1–79, https://doi.org/10.1016/j.pmatsci.2015.12.001.
[22] F. Foroutan, B.A. Ky, I. Abrahams, A. Corrias, P. Gupta, E. Velliou, J.C. Knowles, D. Carta, Mesoporous phosphate-based glasses prepared via Sol−Gel, ACS Biomater. Sci. Eng. 6 (2020), https://doi.org/10.1021/acsbiomaterials.9b01896.
[23] F. Foroutan, B.A. Kyffin, A. Nikolaou, J. Merino-Gutierrez, I. Abrahams, N. Kanwal, J.C. Knowles, A.J. Smith, G.J. Smales, D. Carta, Highly porous phosphate-based glasses for controlled delivery of antibacterial Cu ions prepared via sol-gel chemistry, RSC Adv. 13 (2023) 19662–19673, https://doi.org/10.1039/d3ra02958a.
[24] F. Foroutan, B.A. Kyffin, I. Abrahams, J.C. Knowles, E. Sogne, A. Falqui, D. Carta, Mesoporous strontium-doped phosphate-based sol-gel glasses for biomedical applications, Front. Chem. 8 (2020) 1–8, https://doi.org/10.3389/fchem.2020.00249.
[25] S. Rajadorai, G. Harris, A. Robinson, E.J. Miles, J.M. Roberts, L. Cooper, E.A. Abou Neel, S.M. Higham, N.L. Flannigan, S.P. Valappil, Antibacterial, remineralizing

zinc oxide-doped phosphate-based glasses, Mater. Lett. 306 (2022) 130813, https://doi.org/10.1016/j.matlet.2021.130813.
[26] M. Alqaysi, A. Aldaadaa, N. Mordan, R. Shah, J.C. Knowles, Zinc and strontium based phosphate glass beads: a novel material for bone tissue engineering, Biomed. Mater. 12 (2017), https://doi.org/10.1088/1748-605X/aa8346.
[27] G.J. Smales, B.R. Pauw, The MOUSE project: a meticulous approach for obtaining traceable, wide-range X-ray scattering information, J. Instrum. 16 (2021) P06034, https://doi.org/10.1088/1748-0221/16/06/p06034.
[28] J. Filik, A.W. Ashton, P.C.Y. Chang, P.A. Chater, S.J. Day, M. Drakopoulos, M. W. Gerring, M.L. Hart, O. V Magdysyuk, S. Michalik, A. Smith, C.C. Tang, N. J. Terrill, M.T. Wharmby, H. Wilhelm, Processing two-dimensional X-ray diffraction and small-angle scattering data in {\it DAWN 2, J. Appl. Crystallogr. 50 (2017) 959–966, https://doi.org/10.1107/S1600576717004708.
[29] B.R. Pauw, A.J. Smith, T. Snow, N.J. Terrill, A.F. Thu, The modular small-angle X-ray scattering data correction sequence research papers, J. Appl. Crystallogr. 50 (2017) 1800–1811, https://doi.org/10.1107/S1600576717015096.
[30] I. Bressler, B.R. Pauw, A.F. Thünemann, McSAS : software for the retrieval of model parameter distributions from scattering patterns, J. Appl. Crystallogr. 48 (2015) 962–969, https://doi.org/10.1107/S1600576715007347.
[31] D. Massiot, F. Fayon, M. Capron, I. King, S. Le Calvé, B. Alonso, J.-O. Durand, B. Bujoli, Z. Gan, G. Hoatson, Modelling one- and two-dimensional solid-state NMR spectra, Magn. Reson. Chem. 40 (2002) 70–76, https://doi.org/10.1002/mrc.984.
[32] C.J. Gommes, Stochastic models of disordered mesoporous materials for small-angle scattering analysis and more, Microporous Mesoporous Mater. 257 (2018) 62–78, https://doi.org/10.1016/j.micromeso.2017.08.009.
[33] A. Mufundirwa, Y. Sakurai, M. Arao, M. Matsumoto, H. Imai, H. Iwamoto, Contrast variation method applied to structural evaluation of catalysts by X-ray small-angle scattering, Sci. Rep. 14 (2024), https://doi.org/10.1038/s41598-024-52671-7.
[34] P.I. Ravikovitch, A.V. Neimark, Characterization of micro- and mesoporosity in SBA-15 materials from adsorption data by the NLDFT method, J. Phys. Chem. B 105 (2001) 6817–6823, https://doi.org/10.1021/jp010621u.
[35] L.M. Henning, J.T. Müller, G.J. Smales, B.R. Pauw, J. Schmidt, M.F. Bekheet, A. Gurlo, U. Simon, Hierarchically porous and mechanically stable monoliths from ordered mesoporous silica and their water filtration potential, Nanoscale Adv. 4 (2022) 3892–3908, https://doi.org/10.1039/d2na00368f.
[36] R.A. Pollock, B.R. Walsh, J. Fry, I.T. Ghampson, Y.B. Melnichenko, H. Kaiser, R. Pynn, W.J. Desisto, M.C. Wheeler, B.G. Frederick, Size and spatial distribution of micropores in SBA-15 using CM-SANS, Chem. Mater. 23 (2011) 3828–3840, https://doi.org/10.1021/cm200707y.
[37] L.M. Henning, G.J. Smales, M.G. Colmenares, M.F. Bekheet, U. Simon, A. Gurlo, Synthesis and properties of COK-12 large-pore mesocellular silica foam, Nano Select 4 (2023) 202–212, https://doi.org/10.1002/nano.202200223.
[38] F. Zhang, Y. Yan, H. Yang, Y. Meng, C. Yu, B. Tu, D. Zhao, Understanding effect of wall structure on the hydrothermal stability of mesostructured silica SBA-15, J. Phys. Chem. B 109 (2005) 8723–8732, https://doi.org/10.1021/jp044632+.
[39] F. Foroutan, J. McGuire, P. Gupta, A. Nikolaou, B.A. Kyffin, N.L. Kelly, J.V. Hanna, J. Gutierrez-Merino, J.C. Knowles, S. Yi Baek, E. Velliou, D. Carta, Antibacterial copper-doped calcium phosphate glasses for bone tissue regeneration, ACS Biomater. Sci. Eng. 5 (2019) 6054–6062, https://doi.org/10.1021/acsbiomaterials.9b01291.
[40] C. Paredes, J. Roleček, L. Pejchalová, P. Miranda, D. Salamon, Impact of residual carbon after DLP and SPS-Sintering on compressive strength and in-VITRO bioactivity of calcium phosphate scaffolds, Open Ceramics 11 (2022), https://doi.org/10.1016/j.oceram.2022.100281.